Image-domain multile-material decomposition for dual-energy CT via total nuclear norm and ℓ_0 norm

Qiaoqiao Ding, Tianye Niu, Xiaoqun Zhang* and Yong Long*

***Abstract*—Theoretically two materials with different linear attenuation coefficients can be accurately reconstructed using dual-energy CT (DECT) technique. However, the ability to reconstruct three or more basis materials is clinically and industrially important. We propose a new image-domain multi-material decomposition (MMD) method using DECT measurements. The proposed PWLS-TNV-ℓ_0 method uses penalized weighted least-square (PWLS) reconstruction with three regularization terms. The first term is a total nuclear norm (TNV) that accounts for the image property that basis material images share common or complementary boundaries and each material image is piecewise constant. The second term is a ℓ_0 norm that encourages each pixel containing a small subset of material types out of several possible materials. The third term is a characteristic function based on sum-to-one and box constraint derived from the volume and mass conservation assumption. We apply an Alternating Direction Method of Multipliers (ADMM) to optimize the cost function of the PWLS-TNV-ℓ_0 method. Our results on simulated digital phantom and clinical data indicate that the proposed PWLS-TNV-ℓ_0 method reduces noise and improves accuracy of decomposed material images, compared to a recently proposed image-domain MMD method for DECT.**

I. INTRODUCTION

Dual energy CT (DECT) enhances tissue characterization because it can produce images that separate materials such as soft-tissue and bone. DECT is of great interest in applications to medical imaging, security inspection and nondestructive testing. In principle, only two basis materials can be accurately reconstructed from DECT measurements that acquired at low and high energies. In reality a scanned object often contains multiple basis materials. Many clinical and industrial applications require multi-material images. Spectral CT that acquires multi-energy measurements can be used to achieve multiple basis material images. However, spectral CT requires multiple scans at different energies or expensive specialized scanners, such as energy-sensitive photon-counting detectors. We focus on reconstructing multiple basis material images using DECT measurements available from conventional DECT scanners.

This work is supported in part by NSFC (61501292), Shanghai Pujiang Talent Program (15PJ1403900), Returned Overseas Chinese Scholars Program, 973 Program (2015CB856000) and National Youth Top-notch Talent. This work has been initiated during a stay of Qiaoqiao Ding at Germany funded by the China Scholarship Council, whose support is gratefully acknowledged.

Q. Ding and *X. Zhang (e-mail: xqzhang@sjtu.edu.cn) are with School of Mathematical Sciences and Institute of Natural Sciences, Shanghai Jiao Tong University. 800, Dongchuan Road, Shanghai, 200240, China

T. Niu is with Sir Run Run Shaw Hospital and Institute of Translational Medicine, Key Laboratory of Biomedical Engineering of Ministry of Education, Zhejiang University, Hangzhou, Zhejiang, 310009, China

*Y. Long (e-mail: yong.long@sjtu.edu.cn) is with the University of Michigan-Shanghai Jiao Tong University Joint Institute, Shanghai Jiao Tong University, 800 Dongchuan Road, Shanghai, 200240, China

Mendonca *et al.* [1] proposed an image-domain method that decomposes FBP images at low- and high- energy reconstructed from a DECT scan into multiple images of basis materials. It uses mass and volume conservation assumption, and a constraint that each pixel contains at most three materials out of several possible materials to help solve the ill-posed problem of estimating multiple images from DECT measurements. This method estimates volume fractions of basis materials from linear attenuation coefficients (LAC) pairs at high and low energies pixel by pixel without considering noise statistics and prior information of material images, such as piecewise constant property of material images. Long and Fessler [2] proposed a penalized-likelihood (PL) method with edge-preserving regularizers for each material using similar constraints for MMD from sinogram DECT data. This PL method greatly reduced noise, streak and cross-talk artifacts in the reconstructed basis material images. However, this PL method is computationally expensive mainly due to the forward and back-projection between multiple material images and DECT sinograms at low and high energies. Yang *et al.* [3] proposed a statistical image-domain MMD method that uses penalized weighted least-square (PWLS) reconstruction with edge-preserving (EP) regularizers for each material. This method suppresses noise and improves the accuracy of decomposed volume fractions, compared to the method in [1]. It is computationally more practical than the PL method because it is an image-domain method. The aforementioned three methods loop over material triples from several basis materials of interest, enforce sum-to-one and a box constraint ([0 1]) derived from both the volume and mass conservation assumption [2], and require a criterion to determine the optimal material triplet for each pixel. The edge-preserving regularization for each material does not consider the prior information that different material images have common edges. We call the method in [3] the PWLS-EP-LOOP method hereafter.

In this paper we propose a PWLS-TNV-ℓ_0 method that uses PWLS reconstruction with three regularization terms. The first term is a total nuclear norm (TNV) that accounts for image property that basis material images share common or complementary boundaries and each material image is piecewise constant. The second term is a ℓ_0 norm that encourages each pixel containing a small subset of material types out of several possible materials. The third term is a characteristic function based on sum-to-one and a box constraint derived from the volume and mass conservation. We solve the optimization problem of the PWLS-TNV-ℓ_0 method using the Alternating Direction Method of Multipliers (ADMM, also known as split Bregman method [4]) and its unconstrained sub-

DOI: 10.12059/Fully3D.2017-11-3105002

problems using Singular Value Thresholding (SVT) [5] and Hard Thresholding (HT) [6], [7]. Our results on the simulated digital phantom and clinical data indicate that the proposed PWLS-TNV-ℓ_0 method reduces noise and improves accuracy of decomposed material images, compared to the PWLS-EP-LOOP method.

This paper is organized as follows. Section II describes the PWLS-TNV-ℓ_0 method and the ADMM algorithm that minimizes its cost function. Section III presents numerical experiments and results. Finally, we draw our conclusions in Section IV.

II. Method

A. DECT model

For dual energy CT, we can acquire a two-channel image $\boldsymbol{y} = (\boldsymbol{y}_H, \boldsymbol{y}_L)^T \in \mathbb{R}^{2\times N_p}$, where $\boldsymbol{y}_H, \boldsymbol{y}_L$ are the attenuation maps at high and low energy respectively and N_p is the number of pixels. The attenuation images $\boldsymbol{y}$ are represented by a linear combination of L_0 images, where L_0 is the number of materials. Let $\boldsymbol{x} \in \mathbb{R}^{L_0\times N_P}$ denote the L_0 images to be reconstructed

$$\boldsymbol{x} = \left(\ \boldsymbol{x}_1^T, \boldsymbol{x}_2^T, \cdots, \boldsymbol{x}_{L_0}^T \ \right),$$

and $\boldsymbol{x}_l = (x_{l1}, x_{l2}, ..., x_{ln}, ..., x_{lN_p}) \in \mathbb{R}^{N_p}$ denotes the composition of the l-th materials. Then,

$$\boldsymbol{y} = \begin{pmatrix} \boldsymbol{A}_H\boldsymbol{x} \\ \boldsymbol{A}_L\boldsymbol{x} \end{pmatrix} = \begin{pmatrix} \mu_{1H}, \mu_{2H}, \cdots, \mu_{L_0H} \\ \mu_{1L}, \mu_{2L}, \cdots, \mu_{L_0L} \end{pmatrix} \begin{pmatrix} \boldsymbol{x}_1 \\ \vdots \\ \boldsymbol{x}_{L_0} \end{pmatrix},$$

where μ_{lH} and μ_{lL} denote the linear attenuation coefficient of the l-th material at the high and low energy respectively and $\boldsymbol{A} \in \mathbb{R}^{2\times L_0}$ is the system matrix,

$$\boldsymbol{A} = \begin{pmatrix} \boldsymbol{A}_H \\ \boldsymbol{A}_L \end{pmatrix} = \begin{pmatrix} \mu_{1H} & \mu_{2H}\cdots\mu_{L_0H} \\ \mu_{1L} & \mu_{2L}\cdots\mu_{L_0L} \end{pmatrix}.$$

In practice the system matrix $\boldsymbol{A}$ can be measured in advance, and the acquired attenuation image $\boldsymbol{y}$ is degraded with noise $\boldsymbol{\varepsilon}$ as

$$\boldsymbol{y} = \boldsymbol{A}\boldsymbol{x} + \boldsymbol{\varepsilon}. \tag{1}$$

B. Variational model

In (1), the noise is assumed to be additive white noise, with mean 0 and variance $\boldsymbol{\sigma}_H, \boldsymbol{\sigma}_L$ for high- and low-energy image respectively. The weighted least square of low- and high-energy is used as the data fidelity term:

$$\bar{L}(\boldsymbol{x}) = \frac{1}{2}\|\frac{\boldsymbol{y}_H - \boldsymbol{A}_H\boldsymbol{x}}{\boldsymbol{\sigma}_H}\|_2^2 + \frac{1}{2}\|\frac{\boldsymbol{y}_L - \boldsymbol{A}_L\boldsymbol{x}}{\boldsymbol{\sigma}_L}\|_2^2. \tag{2}$$

The volume fractions $\boldsymbol{x}$ is estimated from the noisy measurements $\boldsymbol{y}_H, \boldsymbol{y}_L$ by minimizing a penalized weighted least square (PWLS) cost function as follows:

$$\hat{\boldsymbol{x}} = \text{argmin}_{\boldsymbol{x}}, \Psi(\boldsymbol{x}) \quad \Psi(\boldsymbol{x}) \triangleq \bar{L}(\boldsymbol{x}) + R(\boldsymbol{x}). \tag{3}$$

We propose to use the following regularization term $R(\boldsymbol{x})$

$$R(\boldsymbol{x}) = \beta_1 R_1(\boldsymbol{x}) + \beta_2 R_2(\boldsymbol{x}) + R_3(\boldsymbol{x}). \tag{4}$$

where the three regularization terms will be explained in the following, and the parameters β_1 and β_2 control the noise and resolution tradeoff.

1) Low rank of image gradient: The first regularization term $R_1(\boldsymbol{x})$ is imposed for the correlation of the composition maps of all the materials. In fact, each region of an object typically contains several materials, and the material images will share the similar boundary structures. The boundary of the objects can be represented by the gradient map of image, and the correlation can be represented by the low rankness of the gradient matrix stacked from all the material images. At each pixel $1 \le j \le N_p$, the generalized gradient matrix for all the materials $(\boldsymbol{D}\boldsymbol{x})_j \in \mathbb{R}^{L_0\times N_d}$ is computed by the finite difference along N_d directions,

$$(\boldsymbol{D}\boldsymbol{x})_j = \begin{pmatrix} (\boldsymbol{J_1x_1})_j & (\boldsymbol{J_2x_1})_j & \cdots & (\boldsymbol{J_{N_d}x_1})_j \\ \vdots & \vdots & \ddots & \vdots \\ (\boldsymbol{J_1x_{L_0}})_j & (\boldsymbol{J_2x_{L_0}})_j & \cdots & (\boldsymbol{J_{N_d}x_{L_0}})_j \end{pmatrix}$$

where $\boldsymbol{J_d x_l}$, for $1 \le d \le N_d$ and $1 \le l \le L_0$ denotes the finite difference in the d-th direction on the image $\boldsymbol{x}_l$. As the boundaries are correlated, we penalize the following term

$$R_1(\boldsymbol{x}) = \sum_{j=1}^{N_P} \|(\boldsymbol{D}\boldsymbol{x})_j\|_* \triangleq \|\boldsymbol{D}\boldsymbol{x}\|_* \triangleq R_{TNV}(\boldsymbol{x}), \tag{5}$$

where the overall matrix $\boldsymbol{D}\boldsymbol{x}$ can be also viewed as a 3D matrix with size $L_0 \times N_d \times N_p$. In fact, $R_1(\boldsymbol{x})$ was proposed as a multi-channel regularization based on *total nuclear variation* (TNV) of Jacobian matrix J in [8].

2) Sparsity: It is assumed that each pixel of $\boldsymbol{y}$ only contains a subset of materials rather than all the materials. If the l-th material is not included in pixel j, the fraction x_{lj} must be 0. Therefore, it is natural to use the ℓ_0 norm, $\|\boldsymbol{x}(:,j)\|_0$, at each pixel, i.e.,

$$R_2(\boldsymbol{x}) = \sum_{j=1}^{N_P} \|\boldsymbol{x}(:,j)\|_0 = \|\boldsymbol{x}\|_0. \tag{6}$$

3) Volume and mass conservation: Both volume and mass are assumed to be conserved for the volume fraction x_{lj} at each pixel j. Thus the third constraint is imposed as

$$\sum_{l=1}^{L_0} x_{lj} = 1, \ a_{lj} \le x_{lj} \le c_{lj}, \ l = 1\cdots L_0. \tag{7}$$

Here, $a_{lj} = 0, \ c_{lj} = 1$. The regularization term R_3 is taken as the characteristic function of S:

$$R_3(\boldsymbol{x}) = \chi_S(\boldsymbol{x}) = \begin{cases} 0, & \boldsymbol{x} \in S \\ \infty, & \text{else}, \end{cases} \tag{8}$$

where $S = \{\boldsymbol{x} : \sum_{l=1}^{L_0} x_{lj} = 1, 0 \le x_{lj} \le 1, j = 1, \cdots, N_p\}$.

C. Optimization Method

1) Equivalent Model: Because (3) is hard to solve directly, we introduce auxiliary variables $\boldsymbol{u} \in \mathbb{R}^{L_0\times N_d\times N_p}, \boldsymbol{v} \in \mathbb{R}^{L_0\times N_p}, \boldsymbol{w} \in \mathbb{R}^{L_0\times N_p}$. Then, our problem can be written as the following equivalent constrained problem:

$$\begin{aligned} \text{argmin}_{\boldsymbol{x},\boldsymbol{u},\boldsymbol{v},\boldsymbol{w}} & \frac{1}{2}\|\frac{\boldsymbol{y}_H - \boldsymbol{A}_H\boldsymbol{x}}{\boldsymbol{\sigma}_H}\|_2^2 + \frac{1}{2}\|\frac{\boldsymbol{y}_L - \boldsymbol{A}_L\boldsymbol{x}}{\boldsymbol{\sigma}_L}\|_2^2 \\ & + \beta_1\|\boldsymbol{u}\|_* + \beta_2\|\boldsymbol{v}\|_0 + \chi_S(\boldsymbol{w}) \\ & s.t. \boldsymbol{u} = \boldsymbol{D}\boldsymbol{x}, \boldsymbol{v} = \boldsymbol{x}, \boldsymbol{w} = \boldsymbol{x}. \end{aligned} \tag{9}$$

Rewrite (9) as

$$\text{argmin}_{\boldsymbol{x},\boldsymbol{z}}\ \bar{L}(\boldsymbol{x}) + R(\boldsymbol{z}) \quad s.t. \quad \boldsymbol{z} = \boldsymbol{K}\boldsymbol{x} \tag{10}$$

where $\boldsymbol{z} \triangleq (\boldsymbol{u},\boldsymbol{v},\boldsymbol{w})^T, \boldsymbol{K} \triangleq (\boldsymbol{D},\boldsymbol{I},\boldsymbol{I})^T$.

2) Alternating Direction Method of Multipliers: To solve the optimization problem in (10), the algorithm Alternating Direction Method of Multipliers (ADMM) (also know as split Bregman [4]) is applied. Given $\boldsymbol{x}^0, \boldsymbol{z}^0, \boldsymbol{p}^0$, ADMM updates the sequence $\boldsymbol{x}^n, \boldsymbol{z}^n, \boldsymbol{p}^n$ by

$$\begin{aligned} x^{n+1} &= \text{argmin}_{\boldsymbol{x}}\ \bar{L}(\boldsymbol{x}) + \langle p^n, \boldsymbol{K}\boldsymbol{x} - \boldsymbol{z}^n\rangle \\ &\quad + \frac{\gamma}{2}\|\boldsymbol{K}\boldsymbol{x} - \boldsymbol{z}^n\|_2^2, & (11)\\ \boldsymbol{z}^{n+1} &= \text{argmin}_{\boldsymbol{z}}\ R(\boldsymbol{z}) + \langle p^n, \boldsymbol{K}\boldsymbol{x}^{n+1} - \boldsymbol{z}\rangle \\ &\quad + \frac{\gamma}{2}\|\boldsymbol{K}\boldsymbol{x}^{n+1} - \boldsymbol{z}\|_2^2, & (12)\\ \boldsymbol{p}^{n+1} &= \boldsymbol{p}^n + \boldsymbol{\gamma}(\boldsymbol{K}\boldsymbol{x}^{n+1} - \boldsymbol{z}^{n+1}), & (13)\end{aligned}$$

where $\gamma > 0$ is the penalty parameter and $\boldsymbol{p} = (\boldsymbol{p}_1, \boldsymbol{p}_2, \boldsymbol{p}_3)^T$, $\boldsymbol{p}_1 \in \mathbb{R}^{L_0\times N_d\times N_p}, \boldsymbol{p}_2 \in \mathbb{R}^{2\times N_p}, \boldsymbol{p}_3 \in \mathbb{R}^{2\times N_p}$ have the same size as $\boldsymbol{D}\boldsymbol{x}, \boldsymbol{x}, \boldsymbol{x}$ respectively. Note that we can also select a vector $\boldsymbol{\gamma} = (\gamma_1, \gamma_2, \gamma_3)$ for the three quadratic penalty constraints.

3) Algorithm: Firstly, we solve (11) to obtain $\boldsymbol{x}^{n+1}$. Since (11) is quadratic and differentiable on $\boldsymbol{x}$, it is equal to solve a linear system, i.e.

$$\begin{aligned} G\boldsymbol{x} &= \frac{1}{\sigma_H^2}\boldsymbol{A}_H^T\boldsymbol{y}_H + \frac{1}{\sigma_L^2}\boldsymbol{A}_L^T\boldsymbol{y}_L + \boldsymbol{D}^T(\gamma_1\boldsymbol{u}^n - \boldsymbol{p}_1^n) \\ &\quad + \gamma_2\boldsymbol{v}^n - \boldsymbol{p}_2^n + \gamma_3\boldsymbol{w}^n - \boldsymbol{p}_3^n, & (14)\end{aligned}$$

where $G = \frac{1}{\sigma_H^2}\boldsymbol{A}_H^T\boldsymbol{A}_H + \frac{1}{\sigma_L^2}\boldsymbol{A}_L^T\boldsymbol{A}_L + \gamma_1\boldsymbol{D}^T\boldsymbol{D} + \gamma_2 + \gamma_3$, whose is of dimension $L_0 \times L_0$.

Due to the structure of $R(\boldsymbol{z})$ and $\boldsymbol{K}$, (12) can be solved separately for $\boldsymbol{u}, \boldsymbol{v}, \boldsymbol{w}$ as follows:

$$\boldsymbol{u}^{n+1} = \arg\min_{\boldsymbol{u}} \beta_1\|\boldsymbol{u}\|_* + \frac{\gamma_1}{2}\|\boldsymbol{u} - \boldsymbol{D}\boldsymbol{x}^{n+1} - \frac{\boldsymbol{p}_1^n}{\gamma_1}\|_2^2, \tag{15}$$

$$\boldsymbol{v}^{n+1} = \arg\min_{\boldsymbol{v}} \beta_2\|\boldsymbol{v}\|_0 + \frac{\gamma_2}{2}\|\boldsymbol{v} - \boldsymbol{x}^{n+1} - \frac{\boldsymbol{p}_2^n}{\gamma_2}\|_2^2, \tag{16}$$

$$\boldsymbol{w}^{n+1} = \arg\min_{\boldsymbol{w}} \chi_S(\boldsymbol{w}) + \frac{\gamma_3}{2}\|\boldsymbol{w} - \boldsymbol{x}^{n+1} - \frac{\boldsymbol{p}_3^n}{\gamma_3}\|_2^2. \tag{17}$$

- We use *Singular Value Thresholding* [5] to solve (15).

$$\boldsymbol{u}^{n+1}(:,:,j) = \mathcal{D}_{\frac{\beta_1}{\gamma_1}}([\boldsymbol{D}\boldsymbol{x}^{n+1} + \frac{\boldsymbol{p}_1^n}{\gamma_1}](:,:,j)), j = 1,\cdots,N_p$$

The singular value thresholding operator, $\mathcal{D}.(\cdot)$, is the proximal operator associated with the nuclear norm. For $\tau \geq 0$ and $\boldsymbol{Y} \in \mathbb{R}^{n_1\times n_2}$, the singular value shrinkage operator obeys

$$\mathcal{D}_\tau(\boldsymbol{Y}) = \text{prox}_{\lambda\|\cdot\|_*}(Y) = \text{argmin}_{\boldsymbol{X}}\ \tau\|\boldsymbol{X}\|_* + \frac{1}{2}\|\boldsymbol{X} - \boldsymbol{Y}\|_F^2.$$

The singular value decomposition (SVD) of $\boldsymbol{Y}$ is

$$\boldsymbol{Y} = \boldsymbol{U}\boldsymbol{\Sigma}\boldsymbol{V}^*,$$

where $\boldsymbol{U} \in \mathbb{R}^{n_1\times r}$, $\boldsymbol{V} \in \mathbb{R}^{n_2\times r}$ with orthonormal columns, and $\boldsymbol{\Sigma} = \text{diag}(\{\sigma_i\}_{1\leq i\leq r})$. We obtain

$$\mathcal{D}_\tau(\boldsymbol{Y}) := \boldsymbol{U}\mathcal{D}_\tau(\boldsymbol{\Sigma})\boldsymbol{V}^*, \tag{18}$$

where $\mathcal{D}_\tau(\boldsymbol{\Sigma}) = \text{diag}(\{\sigma_i - \tau\}_+)$, $\{t\}_+ = \max(0,t)$.

- The closed-form solution for (16) is obtained by

$$\boldsymbol{v}^{n+1} = \mathcal{H}_{\frac{\beta_2}{\gamma_2}}(\boldsymbol{x}^{n+1} + \frac{\boldsymbol{p}_2^n}{\gamma_2}), \tag{19}$$

where $\mathcal{H}.(\cdot)$ is the hard thresholding operator [6], [7]. For nonnegative λ and vector x,

$$\mathcal{H}_\lambda(x) = \text{prox}_{\lambda\|\cdot\|_0}(x) = \text{argmin}_y\ \lambda\|y\|_0 + \frac{1}{2}\|y - x\|_2^2,$$

with

$$(\mathcal{H}_\lambda(x))_i = \begin{cases} x_i & \text{if } |x_i| > \sqrt{2\lambda}, \\ \{0, x_i\} & \text{if } |x_i| = \sqrt{2\lambda}, \\ 0 & \text{if } |x_i| < \sqrt{2\lambda}. \end{cases}$$

- Subproblem (17) is the projection on to a simplex [9], [10],

$$\boldsymbol{w}^{n+1}(:,j) = \mathcal{P}_{1^+}([\boldsymbol{x}^{n+1} + \frac{\boldsymbol{p}_3^n}{\gamma_3}](:,j)), j = 1,\cdots N_p.$$

where $\mathcal{P}$ is a projection operator. For nonnegative λ and vector x,

$$\mathcal{P}_{\lambda^+}(x) = \text{prox}_{\lambda\|\cdot\|_0}(x) = \text{argmin}_y\ \chi_S(y) + \frac{1}{2}\|y - x\|_2^2,$$

where $S = \{x : \sum_i x_i = \lambda, x_i \geq 0\}$. Specifically,

$$(\mathcal{P}_{\lambda^+}(x))_i = \{x_i - \hat{t}\}_+$$

where $\hat{t} := \frac{1}{n-k}(\sum_{j=k+1}^n x_{(j)} - \lambda)$ with $k := \max\{p : x_{(p+1)} \geq \frac{1}{n-p}(\sum_{j=p+1}^n x_{(j)} - \lambda)\}$ and $x_{(1)} \leq \cdots \leq x_{(n)}$ is the permutation of x in ascending order.

Algorithm 1 summarizes the optimization algorithm of PWLS-TNV-L0.

Algorithm 1 PWLS-TNV-ℓ_0

Input. $\beta_1, \beta_2, y_H, y_L, A, \boldsymbol{\gamma}$
Initial $\boldsymbol{p}^0 = (\boldsymbol{p}_1^0, \boldsymbol{p}_2^0, \boldsymbol{p}_3^0,)^T$, $\boldsymbol{u} = \boldsymbol{D}\boldsymbol{x}^0, \boldsymbol{v} = \boldsymbol{x}^0, \boldsymbol{w} = \boldsymbol{x}^0$ Maxiter, tol, $n = 1$
while *error* $>$ tol, n $<$ Maxiter **do**
  Solve linear system (14) by CG.
  $\boldsymbol{u}^{n+1}(:,j,:) = \mathcal{D}_{\frac{\beta_1}{\gamma_1}}([\boldsymbol{D}\boldsymbol{x}^{n+1} + \frac{\boldsymbol{p}_1^n}{\gamma_1}](:,j,:)),\ j = 1\cdots N_p$
  $\boldsymbol{v}^{n+1} = \mathcal{H}_{\frac{\beta_2}{\gamma_2}}(\boldsymbol{x}^{n+1} + \frac{\boldsymbol{p}_2^n}{\gamma_2})$
  $\boldsymbol{w}^{n+1}(:,j) = \mathcal{P}_{1^+}([\boldsymbol{x}^{n+1} + \frac{\boldsymbol{p}_3^n}{\gamma_3}](:,j)), i = 1,\cdots N_p$
  Compute $\boldsymbol{p}_1^{n+1}, \boldsymbol{p}_2^{n+1}, \boldsymbol{p}_3^{n+1}$ base on (13)
  $n = n + 1$ and Compute *error*
end while

III. Results

A. Digital phantom study

To evaluate the proposed PWLS-TNV-ℓ_0 method for MMD, we simulated a DECT scan and reconstructed volume fractions of a modified NCAT chest phantom [11] containing adipose, blood, omnipaque300 (iodine-based contrast agent), cortical bone and air. We compared the PWLS-TNV-ℓ_0 method with the PWLS-EP-LOOP method [3].

Fig.1 (a) shows the true volume fractions of the simulated NCAT chest phantom. The simulated true images were

1024×1024 and the pixel size was 0.49 mm. We generated sinograms of size 888×984 using GE LightSpeed X-ray CT fan-beam system geometry corresponding to a mono-energetic source at 70keV and 140keV with 1×10^5 incident photons per ray without scatter. We used filtered back projection (FBP) to reconstruct attenuation images of size 512×512 with a coarser grid, where the pixel size was 0.98 mm. We implemented the direct inversion MMD method in [1] and used its results as the initialization for the PWLS-EP-LOOP [3] and the proposed PWLS-TNV-ℓ_0 method.

Fig.1 (b) and (c) show the decomposed material images by the PWLS-EP-LOOP and PWLS-TNV-ℓ_0 method respectively. For the PWLS-TNV-ℓ_0 method, we set $\beta_1 = 3$ and $\beta_2 = 10$. The regions of interest (ROI) in the blood and omnipaque300 component image were enlarged and shown at the lower left corners of Fig.1 (b2, c2) and Fig.1 (b3, c3). The PWLS-TNV-ℓ_0 method reduced noise, artifacts and crosstalk in the component images, especially for the adipose, blood and bone image, compared to the PWLS-EP-LOOP method.

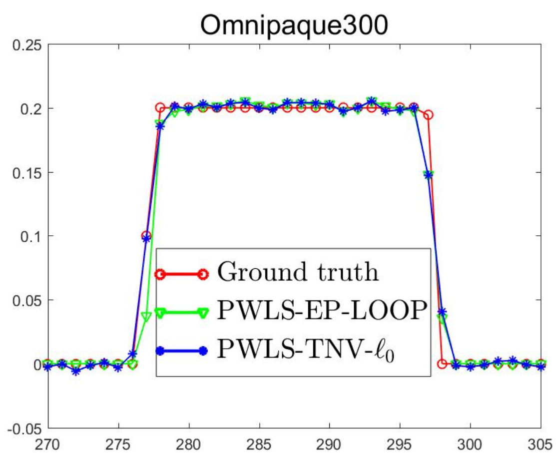

Fig. 2: Profiles of Omnipaque300 images along the labeled red line shown in Fig.1 (a3)

We calculated the Root Mean Square Error (RMSE) and SSIM of the decomposed material images. The RMSE is defined as $\sqrt{\frac{1}{N_p}\sum_{j=1}^{N_p}(\hat{x}_{lj} - x_{lj})}$ where x_{lj} denotes the down-sampled true volume fraction of the l-th material at the j-th pixel location. Table I shows the RMSE and SSIM of component images reconstructed by the PWLS-EP-LOOP and PWLS-TNV-ℓ_0 method. Comparing with the PWLS-EP-LOOP method, the PWLS-TNV-ℓ_0 method lowered the RMSE of adipose, blood, bone component, had similar RMSE for air, and increased RMSE for omnipaque300. In fact, the ROI of Omnipaque300 image is a small region. The structures with very small values outside of ROI lead larger RMSE by our method than RMSE by PWLS-EP-LOOP. Fig.2 shows the profiles of the omnipaque300 images along the red line shown in Fig.1 (a3). PWLS-TNV-ℓ_0 preserves edges more accurately than PWLS-EP-LOOP. The RMSE within the ROI is 30.2×10^{-3} and 41.9×10^{-3} for PWLS-TNV-ℓ_0 and PWLS-EP-LOOP respectively.

Method	PWLS-EP-LOOP		PWLS-TNV-ℓ_0	
	RMSE	SSIM	RMSE	SSIM
Adipose	60.3	0.959	**41.8**	**0.982**
Blood	49.0	0.826	**19.4**	**0.968**
Omnipaque300	**1.3**	**0.999**	2.5	0.992
Bone	28.9	0.959	**27.8**	**0.969**
Air	**23.5**	0.957	23.6	**0.967**
Total	163.0	~	**115.1**	~

TABLE I: Root mean square error (RMSE) error and SSIM of material images reconstructed by different methods. The unit of RMSE is 10^{-3}.

B. Patient Study

The proposed PWLS-TNV-ℓ_0 method is also evaluated using clinical data. The CT images of head patient are shown in Fig. 3.

The bone, iodine, muscle, fat and air were selected as the basis materials. We implemented the direct inversion MMD method in [1] and used its results as the initialization for the PWLS-EP-LOOP [3] and the proposed PWLS-TNV-ℓ_0 method. Fig.4 (a), (b) and (c) show the decomposed material images by the direct inversion, PWLS-EP-LOOP and PWLS-TNV-ℓ_0 method respectively. For the PWLS-TNV-ℓ_0 method, we set $\beta_1 = 1$ and $\beta_2 = 10$. The proposed PWLS-TNV-ℓ_0 method decomposes basis material images more accurately, and decreases crosstalk, especially for the iodine image, compared to the direction inversion method and the PWLS-EP-LOOP method. The PWLS-TNV-ℓ_0 suppresses noise while retaining spatial resolution of the decomposed images.

IV. Discussion and conclusion

We proposed an image-domain MMD method, PWLS-TNV-ℓ_0, using DECT measurements. PWLS-TNV-ℓ_0 method takes low rank property of material image gradient, sparsity of material composition and mass and volume conservation into consideration. We minimize the cost function using ADMM which divides the original optimization problem into several subproblems that are easier to solve. The results on simulated phantom and clinical data show that PWLS-TNV-ℓ_0 reduces noise and crosstalk, compared to PWLS-EP-LOOP. We will investigate acceleration methods to speed up the SVD operation for every pixel in each iteration. PWLS-TNV-ℓ_0 method requires to tune two regularization parameters and several other parameters when optimizing its cost function using ADMM. Future work will discuss how to chose these parameters. The PWLS-TNV-ℓ_0 model assumes the noise variance is uniformly distributed, and estimates it using the measurement inside a manually selected region of homogeneous material [3]. We will investigate estimating noise variance map from projection data [12].

References

[1] Paulo R S Mendonca, Peter Lamb, and Dushyant V Sahani, “A Flexible Method for Multi-Material Decomposition of Dual-Energy CT Images,” *IEEE Transactions on Medical Imaging*, vol. 33, no. 1, pp. 99–116, 2014.

[2] Yong Long and Jeffrey A Fessler, “Multi-Material Decomposition Using Statistical Image Reconstruction for Spectral CT,” *IEEE Transactions on Medical Imaging*, vol. 33, no. 8, pp. 1614–1626, 2014.

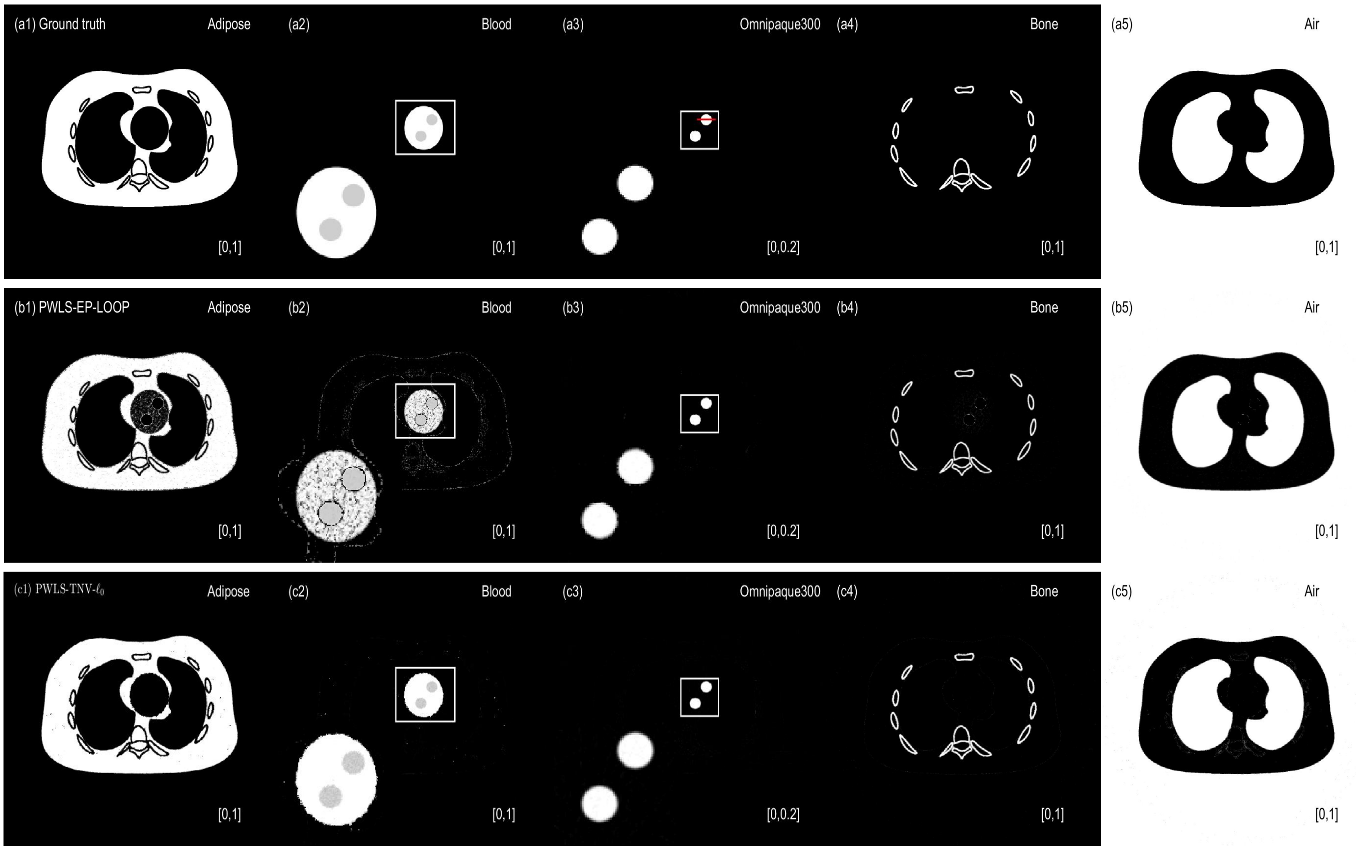

Fig. 1: Material images of ground truth (the 1^{st} row), PWLS-DP-LOOP (the 2^{rd} row) and PWLS-TNV-ℓ_0 (the 3^{nd} row). The display windows are shown in the bottom-right corner.

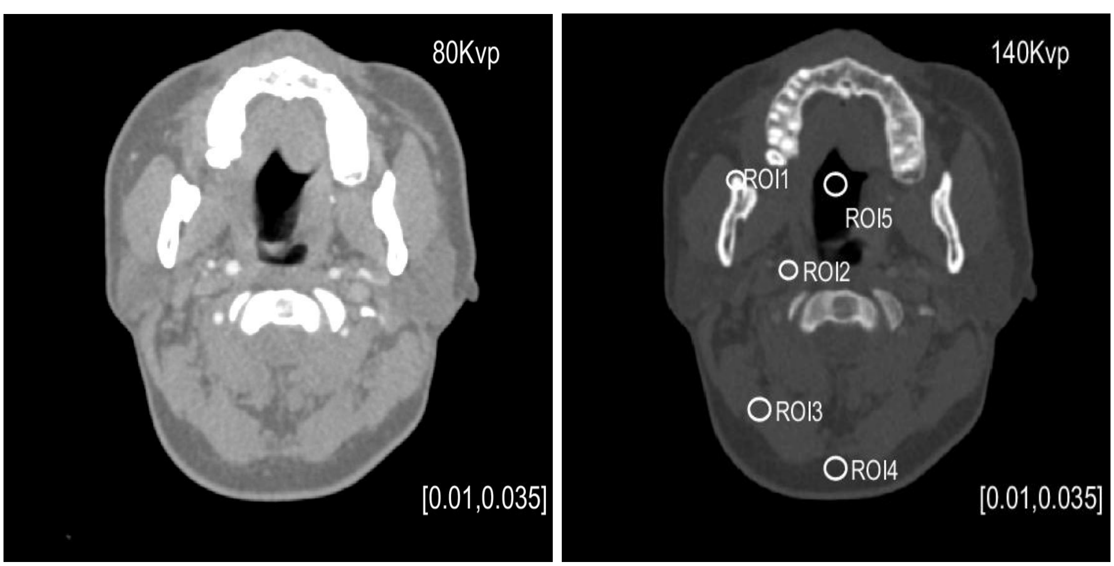

Fig. 3: CT images of a head patient. The major components of ROIs are bone (ROI1), iodine solution (ROI2), muscle (ROI3), fat (ROI4), and air (ROI5), respectively. The display window is [0.01, 0.035] mm^{-1}

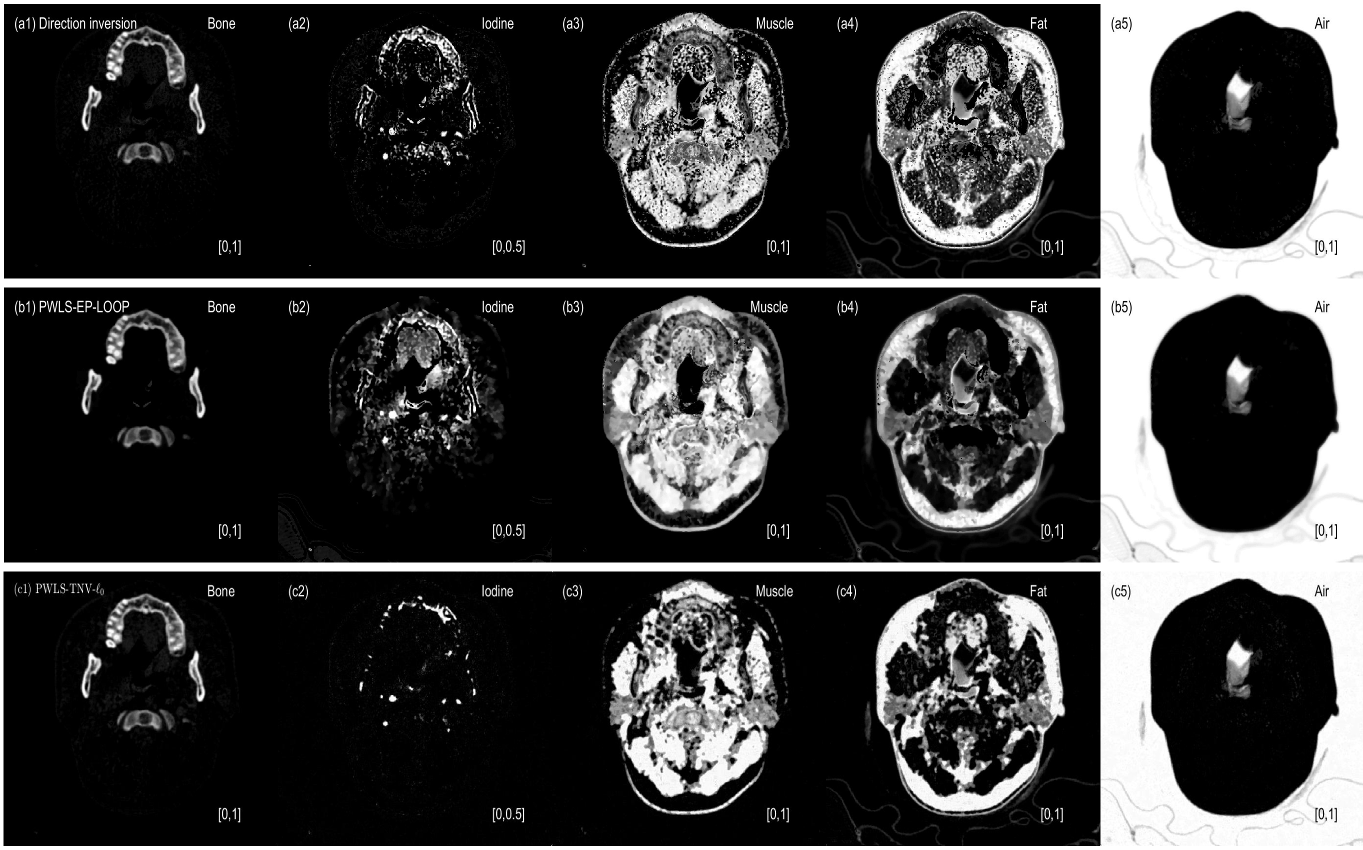

Fig. 4: Material images of the direct inversion method (the 1^{st} row), PWLS-DP-LOOP (the 2^{rd} row) and PWLS-TNV-ℓ_0 (the 3^{nd} row). The display windows are shown in the bottom-right corner.

[3] Yi Xue, Ruoshui Ruan, Xiuhua Hu, Yu Kuang, Jing Wang, Yong Long, and Tianye Niu, "Statistical image-domain multi-material decomposition for dual-energy CT," *Medical Physics*, 2017.

[4] Thomas A Goldstein and Stanley Osher, "The Split Bregman Method for L1-regularized Problems," *SIAM Journal on Imaging Sciences*, vol. 2, no. 2, pp. 323–343, 2009.

[5] Jianfeng Cai, Emmanuel J Candès, and Zuowei Shen, "A singular value thresholding algorithm for matrix completion," *SIAM Journal on Optimization*, vol. 20, no. 4, pp. 1956–1982, 2010.

[6] Thomas Blumensath and Mike E Davies, "Iterative thresholding for sparse approximation," *Journal of Fourier Analysis and Applications*, vol. 14, no. 5, pp. 629–654, 2008.

[7] Joshua D Trzasko, Armando Manduca, and Eric Borisch, "Sparse MRI reconstruction via multiscale l0-continuation," *IEEE/SP 14th Workshop on Statistical Signal Processing*, p. 176C180, 2007.

[8] David S Rigie and Patrick J La Rivière, "A generalized vectorial total-variation for spectral CT reconstruction.," pp. 9–12, 2014.

[9] Anastasios Kyrillidis, Stephen Becker, Volkan Cevher And, and Christoph Koch, "Sparse projections onto the simplex," vol. 28, no. 2, pp. 280–288, 2012.

[10] Yunmei Chen and Xiaojing Ye, "Projection onto a simplex," *arXiv preprint arXiv:1101.6081*, 2011.

[11] William Segars and Benjamin M. W. Tsui, "Study of the efficacy of respiratory gating in myocardial SPECT using the new 4-D NCAT phantom," *IEEE Transactions on Nuclear Science*, vol. 49, no. 3, pp. 675–679, 2002.

[12] Yingying Zhang-O'Connor and Jeffrey A Fessler, "Fast predictions of variance images for fan-beam transmission tomography with quadratic regularization," *IEEE Transactions on Medical Imaging*, vol. 26, no. 3, pp. 335–346, 2007.